Electrochemical activation of a diatom-derived SiO₂/C composite anode and its implementation in a lithium ion battery

Viktor Renman [a],[*], Maria Valeria Blanco [a], Andreas Nicolai Norberg [a], Fride Vullum-Bruer [b], Ann Mari Svensson [a]

[a] Department of Material Science and Engineering, Norwegian University of Science and Technology, NO-7491, Trondheim, Norway
[b] Department of Thermal Energy, SINTEF Energy Research, NO-7034, Trondheim, Norway

ABSTRACT

Nano-architectured silica is extracted from algae harvested in the ocean. Its electrochemical properties are investigated as an anode material for lithium ion batteries. The beneficial effect of a carbon coating formed by pyrolysis of glucose at 850 °C in $Ar_{(g)}$ onto the surface of the SiO_2 particles is demonstrated. The SiO_2 and SiO_2/C composites are characterized by means of SEM, EDX, XRD, FT-IR and Raman spectroscopy, TGA, gas sorption analysis and laser diffraction, in order to verify the structure, morphology and composition of the materials.

A procedure for the electrochemical activation of SiO_2- and SiO_2/C-based electrodes in Li half cells is devised to fully maximize their utility as a host material for Li-ions. The activated SiO_2/C composite reversibly delivers delithiation capacities of ≈ 800 mAhg^{-1} at 50 mAg^{-1} and ≈ 450 mAhg^{-1} at 2000 mAg^{-1} in a LiPF$_6$-carbonate electrolyte. The properties of an electrochemically activated, algae-derived silica-based electrode (SiO_2/C) is investigated in a full cell configuration using a commercially available $LiNi_{0.4}Mn_{0.4}Co_{0.2}O_2$ (NMC442) cathode material. Such a cell operates at an average discharge voltage of 3 V while delivering capacities up to ≈ 150 mAhg^{-1} (NMC), which translate into a specific energy density of ≈ 390 mWhg^{-1}, based on the active materials.

1. Introduction

To date, graphite is the primary choice for the negative electrode in state-of-the-art Li-ion batteries [1–3]. This is mainly due to its number of highly favorable characteristics, which all contribute to exceptional electrochemical properties exhibited by this material. These include a reaction potential close to the Li$^+$/Li redox couple, which is desirable in terms of maximizing the energy density of a battery when coupled to a suitable cathode material. Reversible insertion of Li-ions is made possible through an *intercalation* mechanism which results in a moderate volume expansion of 9%. The well-ordered layered arrangement of graphene sheets in its crystal structure provide high electronic conductivity which enhances electron transfer and enables fast reaction kinetics with Li-ions. The theoretical specific gravimetric capacity is 372 mAhg^{-1} for a fully lithiated Li$_x$C$_6$ compound, where $0 < x \leq 1$. Hence, graphite cannot accommodate more than one e$^-$ plus one Li$^+$ per formula unit so its electrochemical energy storage capacity is inherently limited [4–6]. Furthermore, concerns have been raised recently over graphite by European Union directives by virtue of its role as a critical

raw material in the transition to a low-carbon economy [7–9].

Accordingly, alternative elements and compounds are currently being explored to develop materials which involve multielectron transfer that can potentially boost the energy storage capacity of such anodes. Two major categories of reactions have been identified as alternatives to intercalation of Li into graphite, namely electrochemical *alloying* between Li and metals [10] (*e.g.,* Al, Zn, Ag *etc.*) or semimetals (*e.g.,* Si, Ge, *etc.*) as well as *conversion* reactions [11–13] of various metal compounds (*i.e.,* MX where X = O, P, N, S, *etc.*). Both classes of reactions demonstrate the ability to deliver high Li-storage capacities by virtue of the high number of electrons involved in their respective processes. However, an array of other crucial issues (*i.e.,* limited electronic conductivity, severe volume changes, destruction of the host structures *etc.*) are unavoidable by the intrinsic properties of these reactions.

This study investigates silica frustules (*i.e.,* silica shells) derived from harvested algae naturally occurring in the ocean, and their electrochemical properties as an anode material for Li-ion batteries. Early studies dismissed SiO_2 as a candidate electrode material for Li-ion batteries since it was believed to be practically inert toward Li [14]. This

---

initial judgment was justified as bulk SiO_2 particles exhibit low electrical conductivity and sluggish diffusivity of Li-ions. Hence, under conventional experimental lithiation procedures in Li half cells the bulk silica particles will not allow an electrochemical reaction with Li-ions to penetrate beyond a depth of only a few nanometers [15], thereby yielding a limited electrochemical storage capacity (typically ~150–200 mAh g^{-1} depending on electrode engineering parameters). Later studies found that SiO_2 nanoparticles [16] exhibited significantly higher activity toward Li which, in turn, has sparked renewed interest in SiO_x and SiO_2-based composite materials as a cheap, abundant and environmentally friendly negative electrode material for Li-ion batteries. [17] Besides nano-sizing, further measures to enhance the electrochemical activity of SiO_2-based materials (and conversion materials in general) include the application of carbon-coatings that increase the electronic conductivity [18–24]. A conductive carbon matrix may also have the additional beneficial effect of alleviating the stress and strain associated with its expansion and contraction upon repeated electrochemical insertion and removal of Li-ions [25–29]. Further alleviation of such stresses are speculated to be provided by an intrinsic property of SiO_2 itself, namely its tendency to undergo an *in-situ* formation of a complex nanocomposite comprised of both active and inactive components during lithiation.

The electrochemical reaction mechanism of SiO_2 with Li-ions is complex. Theoretical calculations suggest that formation of $Li_2Si_2O_5$ is energetically most favorable during uptake of Li-ions and a reaction should take place at $\approx$1.3 V *vs.* Li$^+$/Li [30]. Moreover it was suggested that other silicates (*e.g.,* Li_4SiO_4 and Li_2SiO_3) forms in a voltage range of $\approx$1.15–1.25 V *vs.* Li$^+$/Li while formation of Li_2O only becomes possible below $\approx$0.7 V *vs.* Li$^+$/Li. In practice, huge overpotentials (>1 V) are commonly observed due to strong kinetic limitations. Experimentally, it is generally accepted that $Li_2Si_2O_5$, Li_4SiO_4, Li_2O and Li_xSi are formed at some point during lithiation, but there are large variations in electrochemical behavior between different studies, depending on particle and electrode engineering. Although there is still some debate over which reaction pathways are active, a consolidated reaction mechanism in which SiO_2 is electrochemically reduced at low potentials *vs.* Li$^+$/Li has gradually emerged [16,31–33]. It involves disproportionation of the parent compound into $Li_2Si_2O_5$ and Li_4SiO_4 along with the displacement of elemental Si. For the application of SiO_2 in batteries, the highest theoretical capacities are obtained upon complete reduction into elemental Si along with the formation of Li_2O, which is energetically expensive. In practice, it is possible that all of the mentioned compounds are formed to some extent [31]. The Si nanoclusters that are formed as a result of the previously mentioned reaction pathways can then proceed to react further with Li-ions according to the well-known electrochemical alloying process [10,34]. The latter reaction is the biggest contributor to the reversible capacity of SiO_2-based electrodes, with estimated values ranging from $\approx$750–1600 mAh g^{-1} [31]. In other words, SiO_2 combines both *conversion* and *alloying* processes. The reader is referred to the supporting information for a more complete account of the proposed reaction formulas and their associated Li-storage capacities.

SiO_2 derived from diatom frustules has previously been investigated as an anode material in Li half cells. An initial study demonstrated a reversible capacity of 500 mAh g^{-1} after 80 cycles for a composite material obtained by pyrolysis of red algae covered by diatoms [35]. A later study used the native organic matter to coat the diatoms *via* pyrolysis at 900 °C, which yielded a crystalline SiO_2/C composite that delivered a specific capacity of 521 mAh g^{-1} between 5 mV and 3.0 V *vs.* Li$^+$/Li [36]. A third study looked at electrodes with amorphous diatoms and carbon black in a 1:1 ratio which resulted in specific capacities of 400 ± 9 mAh g^{-1} over 90 cycles [37]. More recently, carbon-coated *Coscinodiscus* diatoms were obtained *via* pyrolysis of sucrose at 650 °C. The amount of highly porous carbon in such a SiO_2/C composite was 46.5% by weight. Composite electrodes with 35% carbon black added had an effective SiO_2 content of $\approx$27 wt-% and delivered a reversible capacity of 723

mAh g^{-1} after the inclusion of a potentiostatic lithiation step at a low voltage which enhanced the capacity [38].

Here, silica is obtained from naturally occurring raw material. The extracted product is characterized *via* an array of characterization techniques. The nanostructured silica is processed further in order to achieve control of particle size and morphology. Glucose is utilized as a precursor to achieve a carbon-coating onto the silica particles by means of pyrolysis at high temperature in an inert atmosphere. The electrochemical properties of the resulting amorphous SiO_2/C composite are tested in Li half cells and a comparison to non-coated silica is made to further investigate the effect of the conductive additive. The electrodes and active material in previous studies on diatoms in the context of Li-ion batteries typically have a very high carbon content. In the present work, an effort has been made to significantly increase the relative amount of silica within the composite electrodes in order to achieve slightly more realistic proportions.

To elucidate the true potential of this particular silica as an electrode material, anodes have been tested in a full cell, in combination with a cathode fabricated from commercially available NMC-442. The composition of the anodes were 75 wt% silica derived from diatom frustules, 10 wt% carbon black and 10 wt% binder, thus the silica was the main active material. Pre-lithiation is required in order to avoid excessive lithium consumption from the conversion reactions, and an electrochemical pre-lithiation procedure was optimized to ensure a high degree of conversion prior to the full-cell tests. The electrochemical pre-lithiation procedure was compared to an internal short-circuiting procedure, involving direct exposure of the silica electrode to metallic lithium. The effect of carbon coating on the pre-conditioning procedure is also studied. The results from the full cell experiments verifies the advantages of the material, namely the high stability and high capacity of the anodes, although dominated by lithiation and delithiation of silicon, and illustrates the challenges that still needs to be overcome, in particular with respect to energy efficiency, for future use in large scale.

2. Experimental

2.1. Recovery and processing of biomineralized silica from algae

Coscinodiscus diatoms (Planktonic AS) harvested from the ocean were washed using deionized water to remove sea salt and other possible water-soluble contaminants. After drying the washed diatoms at 150 °C, the algae were placed in a crucible and later calcined at 650 °C for 6 h in air to combust the organic part of the diatoms, thereby leaving purified biomineralized silica frustules as the final product.

The recovered frustules were crushed to reduce their average particle size, thereby facilitating electrode preparation (see Section 2.3). A few grams of frustules were placed in a tungsten carbide (WC) jar together with hundreds of WC balls (φ3 mm diameter). The ball-to-powder mass ratio was *ca.* 20:1. Ethanol was added to the jar as a milling medium. A planetary mill (Retsch PM100) operating at 400 rpm for a couple of hours yielded a powder with a significantly reduced average particle size. Such harsh milling conditions were necessary since the 3D microstructure of Coscinodiscus has been shown to be mechanically resilient [39].

Some of the milled frustules were carbon coated to enhance the electrochemical utilization of the material by increasing the electronic conductivity of the resulting composite. The particles were ultrasonically dispersed in an aqueous solution of glucose (40 wt-% with respect to the silica). The mixture was kept agitated until evaporation of excess water was complete. The silica-glucose mixture was then heat treated at 850 °C under a flow of Ar$_{(g)}$ in order to pyrolyze the carbon.

2.2. Materials characterization

The morphological features of the extracted and milled frustules were examined by scanning electron microscopy (SEM, Zeiss Ultra 55).

Additional estimations of the particle size distributions were obtained *via* laser diffraction. A Horiba Partica LA-960 particle size analyzer employing a 650 nm laser diode (5 mW power) and a 405 nm LED (3 mW) provided volumetrically based particle size distributions on the basis of the refractive index of quartz in water. Prior to the measurements, powder samples were dispersed in water *via* rigorous ultrasonication.

Surface areas and pore structures of the prepared samples were further estimated *via* N_2 gas adsorption analysis at 77 K (*i.e.,* $N_{2(l)}$) by employing a Micrometrics Tristar 3000 area and porosity analyzer. All powder samples were thoroughly degassed at an elevated temperature of 250 °C prior to gas sorption analysis.

Fourier Transform Infrared (FTIR) spectroscopy was conducted using a Bruker Vertex 80v spectrometer in attenuated total reflectance (ATR) mode. The spectra were collected in the region between 350 and 4000 cm^{-1} by the cumulative acquisition of 50 scans (4 cm^{-1} resolution). To further investigate the presence of water and hydroxyl groups, additional measurements were recorded in the spectral range of 3000–4000 cm^{-1} using Diffuse Reflectance Infrared Fourier Transform (DRIFT) mode, which enhances the signal-to-noise ratio of the spectral features of the species in this energy range.

Raman spectroscopy was conducted with a WITec alpha300 R confocal spectrometer using an excitation wavelength of 532 nm generated by a solid-state laser diode. The spectrometer was calibrated using a Si wafer prior to analysis. The laser beam was focused on the sample surface by a $100\times$ magnification objective and the measurements were conducted by applying a constant laser power of 6 mW.

The elemental composition of pristine frustules was determined using inductively coupled plasma mass spectrometry (ICP-MS, ALS Scandinavia, Luleå, Sweden) on frustules dissolved in $HNO_3/HCl/HF$ solution.

Powder x-ray diffraction (PXRD) was utilized in order to investigate the crystallinity of the extracted frustules and to ensure the successful removal of crystalline sea salt. The measurements were performed in Bragg-Brentano geometry using a Bruker D8 Focus diffractometer equipped with a LynxEye SuperSpeed detector and employing CuK_α radiation (*i.e.* $\lambda = 1.54$ Å).

2.3. Electrode preparation & electrochemical testing

Composite electrodes were prepared by tape-casting electrode slurries onto Cu foil (18 μm thickness, Schlenk). The slurry composition was 75% active material (SiO_2 or SiO_2/C frustules), 10% carbon black (Timcal, C-NERGY C65) conductive additive and 15% Na-Alginate (Sigma Aldrich) as a water-soluble binder. The binder solution was prepared separately by dissolving Na-Alginate in deionized water. Silica and carbon black were subsequently added to a steel jar together with the appropriate amount of binder solution. The mixture was homogenized utilizing a radially oscillating mixer (RETSCH MM400) operating at 25 Hz for 45 min. The viscous slurry was spread on to the Cu foil current collector by means of a coating machine (KR – K Control Coater) equipped with a wire-wound rod, yielding a wet-film thickness of *ca.* 60 μm. After allowing excess water to evaporate at room temperature, the cast was dried in a convection oven at 60 °C. Circular electrodes were punched using a purpose-built perforator (Hohsen). Such electrodes had a typical active mass loading of ≈0.4–0.5 mg cm^{-2} and a thickness of ≈10 μm as determined using a digital caliper. Due to the electronically insulating nature of silica, such thin electrodes allow for a more focused investigation of its electrochemical properties while simultaneously minimizing the influence of kinetic effects which could arise from an increased electrode thickness. The electrodes were dried in vacuum at 120 °C and were finally kept in an Ar-filled glovebox ($O_2 < 0.1$ ppm, $H_2O < 0.1$ ppm) prior to cell assembly. NMC-442 ($LiNi_{0.4}Mn_{0.4}Co_{0.2}O_2$, BC-723 K, 3 M) cathodes for full cell testing were prepared in an analogous way. Electrode slurries comprising 80% NMC, 10% carbon black and 10% PVDF binder (polyvinylidene, Arkema) dissolved in NMP were cast onto a 15 μm thick Al foil (Hydro).

Stainless steel coin cells (CR2016, Hohsen) were assembled in said glovebox. The cells comprised the silica-based working electrode, a thin porous membrane (Celgard 2400) as a separator, as well as metallic lithium (Sigma Aldrich) as a combined counter- and reference electrode. The electrolyte (Sigma Aldrich) was a solution of 1 M $LiPF_6$ in dissolved in a (1:1 v/v) mixture of ethylene carbonate (EC) and diethyl carbonate (DEC).

Electrochemical tests on the silica-based electrodes were carried out using a BCS 805 multi-channel potentiostat (Bio-Logic) by applying constant current densities in the range of 50 to 2000 mAg^{-1}, where the magnitude of the current is specified with respect to the amount of active material in the composite electrodes. The upper voltage cut-off was set to 2.0 V *vs.* Li$^+$/Li while the lower cut-off was set to 2 mV *vs.* Li$^+$/Li in order to provide a strong driving force (*i.e.,* reducing environment) for lithiation. Additional experimental conditions include potentiostatic holding steps at the end of each reduction (lithiation) or oxidation (delithiation) cycle to carefully monitor the current response of the cell during these particular electrochemical processes. An alternative attempt to activate the SiO_2/C composite was made by internal short circuiting, in which a silica-based electrode was put in direct contact with Li metal (with added electrolyte) for several days in order for a reaction to take place.

NMC cathodes were galvanostatically cycled in Li half cells in a voltage range of 4.3–3.0 V *vs.* Li$^+$/Li using current densities of 15 and 150 mAg^{-1}. Full cells were assembled by taking a pre-conditioned silica-based anode and pairing it with an NMC cathode. The capacities of the anode and cathode were approximately equal, having a negative to positive ratio of N/P ≈ 1.

3. Results and discussion

3.1. Physicochemical properties of extracted frustules

A series of SEM images depicting the as-extracted frustules are presented in Fig. 1. Some of the frustules remain intact, *i.e.* the large hierarchical structures (>100 μm) are still observable after processing (Fig. 1a), although in some cases it appears that parts of the larger structures have been broken up into smaller fragments or flakes (Fig. 1b). The morphology of the particles indicate that *Coscinodiscus* was the predominantly featured diatom species present in the sample used for extraction of silica. For the sake of clarity, it should be stressed that the procedure for extracting purified silica frustules was not designed with the intention of being non-destructive with respect to the large capsule-like architecture. From the perspective of electrode manufacturing, such large particles are not compatible with the stated requirement of producing thin electrodes. Alternative chemical routes to extract intact frustules are reported elsewhere [40,41]. The question of what happens to the nanometric features of the frustules during baking/calcination, however, remains as a question of high importance. A previous study on the thermal behavior of diatom frustules demonstrated that the morphology of such particles may deform significantly when subjected to high temperature calcination [42]. Upon closer inspection of the more intricate features of the frustules here, it is apparent that frustules obtained from this sample are able to withstand a baking temperature of 650 °C without deformation taking place, see Fig. 1c, d. Preservation of the nano-scale building blocks is desired for electrochemical purposes in terms of providing short migration paths for Li-ions within the solid material.

Additional physicochemical analysis results are summarized in Fig. S1 (Supplementary information). The X-ray diffractogram displayed in Fig. S1a highlights the absence of sharp peaks which is evidence of a lack of long-range periodic atomic ordering in the material as well as the successful removal of sea salt from the sample. Frustules obtained from alternative sources, such as diatomaceous earth or other diatom species may be crystalline. The amorphous nature of the current sample may
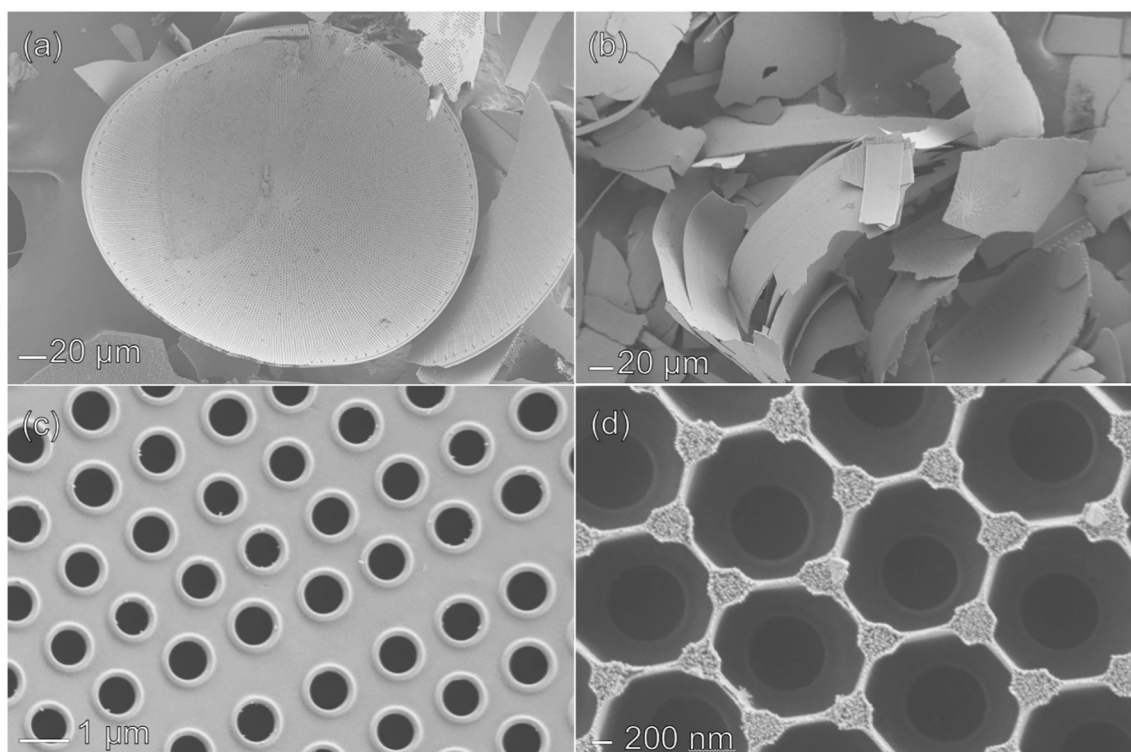
Fig. 1. SEM images of the as-extracted diatom frustules. (a, b) Low-magnification images displaying both intact frustules and frustules broken up into several thin flakes. (c, d) Closer views of typical frustule walls displaying the regular pattern and intricate structural features which result from biomineralization.

have favorable implications in terms of its lithiation properties [43]. FTIR and Raman analyses confirm that the material is silica, see Fig. S1b–d.

Elemental composition analysis by ICP-MS yielded a Si content of 97.86 at-%, whereas other elements such as Na, Mg, Al, P, K, Ca and Fe made up the remainder. Each of the latter made individual contributions of less than 1 at-% (oxygen not included).

3.2. Further processing of the frustules

To facilitate the production of thin electrodes, the frustules were crushed by means of ball milling. The effect of milling on the size distribution and gas sorption properties of the silica particles is summarized in Fig. 2. The as-extracted ("pristine") frustules have a median particle size of $D_{50} \approx 36$ μm with additional distribution parameters of $D_{90} \approx 70$ μm and $D_{10} \approx 10$ μm, respectively, see black/grey traces in Fig. 2a. The milled or crushed silica particles have an estimated median particle size of $D_{50} \approx 280$ nm (blue traces, Fig. 2a) with additional values of $D_{90} \approx 140$ nm and $D_{10} \approx 650$ nm. These numbers along with a visual inspection of the curves in Fig. 2a, indicate that the particle size distribution is shifted by roughly two orders of magnitude in the milling process. It should be stressed that the particle size distribution is still rather wide in both cases. However, it makes sense to observe a wide distribution since a naturally harvested material is likely to display natural variations. Additionally, the original frustules are comprised of a hierarchical architecture which contains structural features that span from both short (a few nanometers) to long length scales (tens of micrometers). As such, it could be conceived that crushing the frustules to some extent "release"
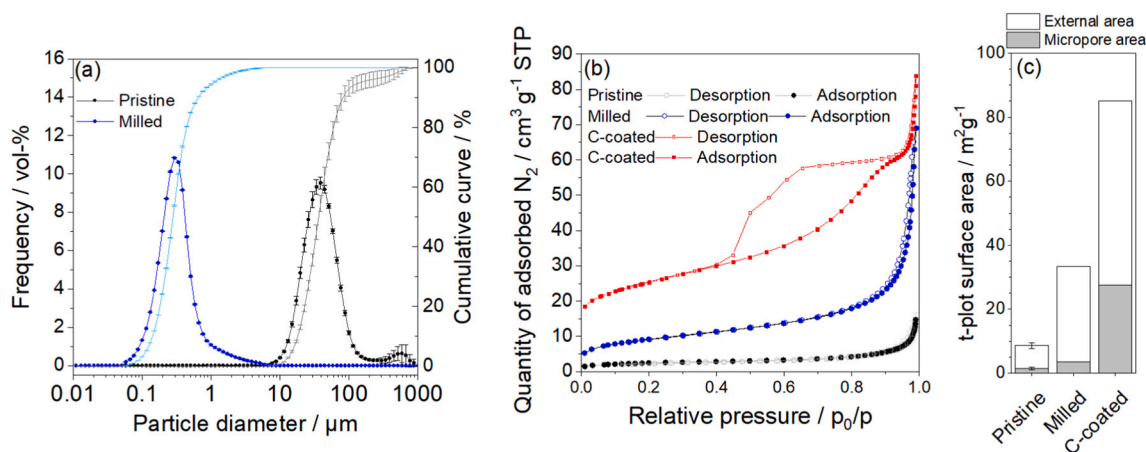
Fig. 2. Summary of particle size and gas sorption analysis. (a) Particle size distributions of milled and pristine frustules. (b) Nitrogen gas adsorption isotherms of pristine (black), milled (blue) and milled/C-coated frustules (red). (c) Surface areas of the particles divided into contributions from both external and micropore surface areas. (For interpretation of the references to colour in this figure legend, the reader is referred to the web version of this article.)

the finer constituents *via* fragmentation of the larger flakes.

The results of gas sorption analysis are summarized in Fig. 2b, c. The pristine frustules give rise to a typical Type II isotherm representative of a macroporous or non-porous material. These findings are in concordance with the morphological study (*c.f.,* Fig. 1) in which macropores and relatively smooth surfaces are immediately visible. Although the frustules partly consist of small, nanometric features such as thin walls, it appears they are not particularly porous. The total surface area of the pristine frustules was estimated to ≈ 8.6 m^{2}g^{-1} using *BET* analysis applied to the adsorption isotherm. Further insights into the pore structure of the powder was provided by additional analysis according to the *t-plot* method, which indicate that the contribution from micropores is ≈ 1.4 m^{2}g^{-1} whereas the external surface area accounts for the remaining ≈ 7.2 m^{2}g^{-1}. The milled frustules also exhibit a typical Type II gas sorption isotherm, with a *BET* surface area of ≈ 33.3 m^{2}g^{-1}. Milling thus increases the surface by more than a factor of four. Further *t-plot* analysis show that the overall increase is primarily attributed to an increase in external surface area (≈ 29.8 m^{2}g^{-1}). While the microporosity increases as well (≈ 3.5 m^{2}g^{-1}), it clearly does so to a relatively lesser extent. The milled and carbon coated sample, on the other hand, exhibit a different gas sorption behavior. The isotherm is described as Type IV. During adsorption, the initial *S*-shaped behavior is similar to both of the previous cases with the exception that there is an additional inflection at higher pressures which indicates capillary condensation takes place in the pores. A hysteresis effect is observed during gas desorption, which in turn points to the presence of a mesoporous structure. According to *BET* analysis of the isotherms of the carbon-coated powder, the total surface area is ≈ 85.1 m^{2}g^{-1}. Here, the contributions are ≈ 27.4 m^{2}g^{-1} from micropores and ≈ 57.7 m^{2}g^{-1} from external surface area, respectively. The reader is referred to the supporting information for a further elaboration on the pore size distributions of the various samples. In the context of electrochemical performance as an electrode material that can react reversibly with Li-ions, such differences observed between the non-coated and C-coated samples are bound to have a significant effect in terms of accessible electrochemically active surface area but also in terms of the extent to which side reactions occur.

Additional SEM analyses were performed to investigate the effect of carbon coating on the particle morphology. A comparison is shown in Fig. 3a, b, where the non-coated and the coated samples appear to be visually similar at a first glance. Obviously, the average size of the silica particles in both samples remains the same, but it is worth noting that the presence of carbon does not appear to alter the morphology on a *μm*-scale, for instance *via* excessive particle aggregation. Ultrasonication and continuous agitation of the glucose-silica slurry ensures a homogeneous distribution of glucose on the surface of the particles, which yields a thin, porous carbon coating during pyrolysis that hinders excessive particle aggregation/sintering. Some of these aspects and considerations have been elaborated upon further in a recent study [44]. Additional energy-dispersive x-ray spectroscopy measurements in the SEM confirmed the even distribution of the carbon coating. Elemental maps of the composite material are displayed in Fig. 3c. The signal of Si (K$_\alpha \approx 1.74$ eV) is shown in red, and the signal of O (K$_\alpha \approx 0.53$ eV) is shown in green. A side-by-side comparison of the two maps shows the expected result that the signals from both elements are neatly overlapping. The distribution of carbon (K$_\alpha \approx 0.28$ eV) is shown as a yellow signal. Note that the carbon signal is weak since it is the lightest element in the sample, and it is present in a relatively small amount. Its presence and its distribution as a thin coating on the silica particles is further highlighted in Fig. S3. The effective carbon content after pyrolysis was 15.4 wt-%, as determined by the change in mass using thermogravimetric analysis (not shown) conducted by means of combustion in air.

3.3. Electrochemical activation in half cells

The electrochemical activation procedure described here is a sequence of constant current (CC) and constant voltage (CV) steps, which altogether provide a slow but steady activation that can be monitored *in situ*. The process is summarized in Fig. 4 where the carbon-coated frustules are used as an example. Slow galvanostatic cycling in a Li half-cell at 50 mAg^{-1} during the first lithiation step ensures a gradual formation of an SEI layer which is homogeneous in terms of its thickness as well as its distribution within the composite electrode. By holding the voltage constant at 2 mV *vs.* Li$^+$/Li a strong driving force (*i.e.*, reducing environment) for lithiation of silica is provided. Furthermore, the long duration (*i.e.*, 48 h) of the constant voltage step gives the Li-ions sufficient time to penetrate the silica beyond the shallowest outer layers of the particles. This effect is clearly visible in the current response during the CV step, where a delayed reaction is observed after *ca.* 15 h at 2 mV
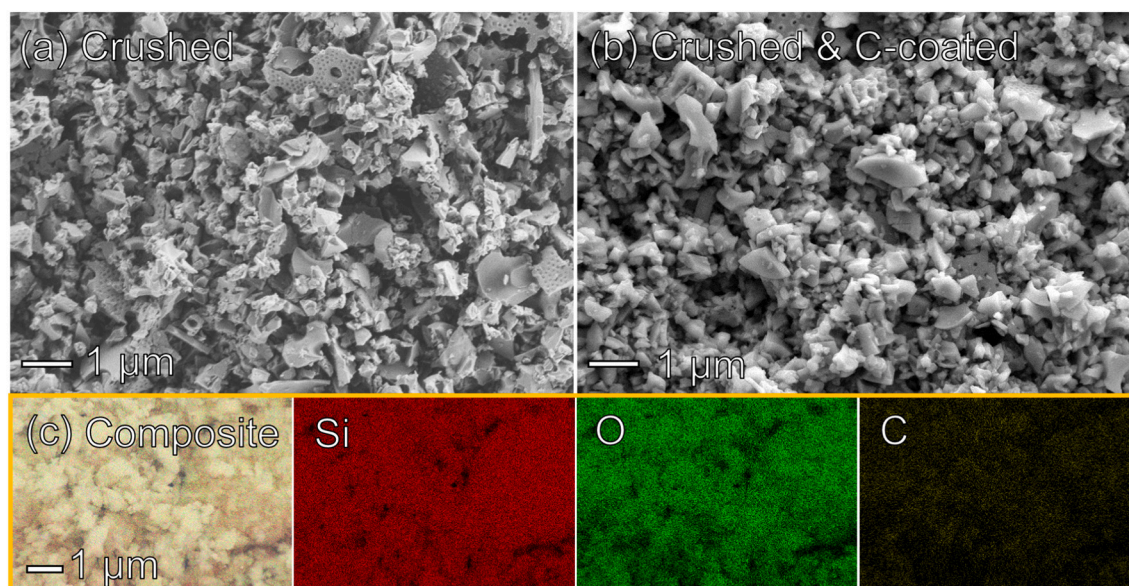
Fig. 3. SEM images of frustules which have been processed further by means of ball-milling and carbon coating. (a) Milled frustules (b) Milled and carbon-coated frustules. (c) Elemental EDX maps of the carbon-coated sample. Red indicates the presence of silicon, while green shows the distribution of oxygen. The signal arising from carbon is displayed in a yellow colour. The composite image shows a superimposition of all elements. (For interpretation of the references to colour in this figure legend, the reader is referred to the web version of this article.)
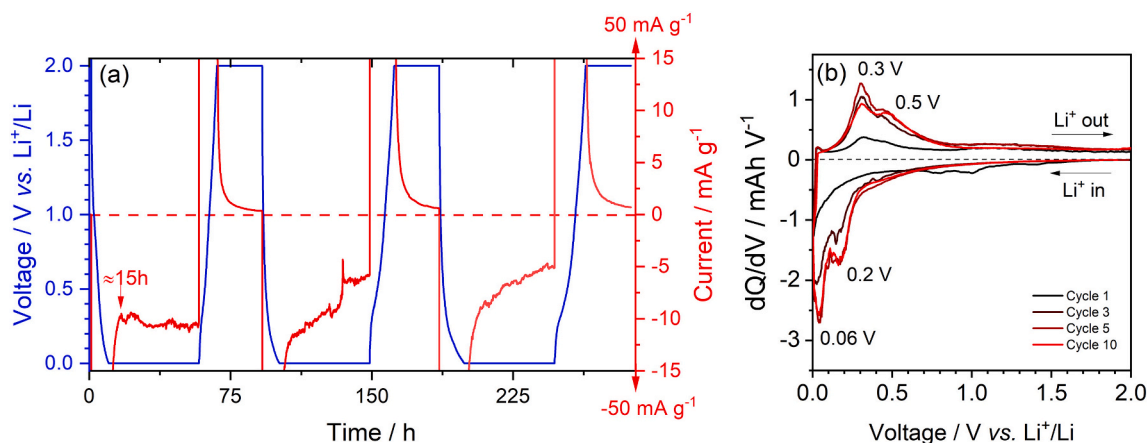
Fig. 4. An example displaying the electrochemical activation procedure in a summarized format. Here, C-coated frustules are used. (a) The voltage profile (blue) along with the current (red) during the first three cycles of the activation process. (b) Differential capacity plots for a selection of cycles highlighting the gradual appearance of features at voltages associated with the reaction of Li-ions with silicon. (For interpretation of the references to colour in this figure legend, the reader is referred to the web version of this article.)

vs. Li$^+$/Li as evidenced by a gradual increase in magnitude of the measured current. The current fluctuates somewhat during the first CV steps(s) which could possibly be attributed to cracking of the SEI layer along with additional electrolyte decomposition as the particles expand when they become lithiated. In total, it was possible to lithiate the electrode to a capacity of $\approx$1000 mAhg^{-1} in the combined CC/CV procedure, which in turn corresponds to an uptake of $\approx$2.2 Li per formula unit of SiO$_2$. Subsequently, CC delithiation was performed at 50 mAg^{-1} up to a voltage cut-off of 2 V *vs.* Li$^+$/Li followed by an immediate CV holding step for 24 h during which the current practically drops to zero relatively quickly, indicating that the procedure ensures complete delithiation. This cycling protocol of alternating slow CC and CV steps allows the active parts of the electrode material to undergo reconstruction in terms of Li migration within the nanoparticles, thereby enhancing the degree of electrochemical utilization. On the other hand, it must be noted that the irreversible capacity loss during the first cycle is a staggering 48%, reflecting the fact that a significant amount of Li is trapped in the form of Li$_2$O, Li$_4$SiO$_4$ and as a significant constituent of the SEI as well. Such irreversible losses are clearly a consequence of the intrinsic reaction mechanism which produces both active and inactive compounds. Furthermore, a rather porous carbon coating within the composite electrodes consumes plenty of the Li inventory due to its high surface area. Further optimization of the electrode composition with respect to the amount of carbon black and binder as well as using electrolyte additives may lead to significant improvements in terms of mitigating irreversible capacity losses (ICL) here. Nevertheless, significant ICL remain as one of the main challenges of silica-based anodes and conversion-based electrode materials in general [17].

In the second lithiation/delithiation cycle, the voltage profile adopts a slightly more well-defined quasi-plateau below 0.3 V *vs.* Li$^+$/Li during the CC lithiation step. The amount of Li inserted in CC mode corresponds to a gravimetric capacity of only $\sim$450 mAhg^{-1}. However, after the transition from CC to CV at 2 mV in the second cycle, the measured current response indicates that the electrode material is more readily lithiated (albeit still slowly) as compared to the first cycle since partial activation has already been achieved. Once again, fluctuations in the magnitude of the measured current are observed for reasons discussed previously. The total amount of Li inserted in the combined CC and CV steps in the second cycle corresponds to a capacity of $\approx$930 mAhg^{-1}. During the second delithiation in CC mode, the voltage profile now exhibits a significantly more pronounced plateau-like feature centered at around 0.3–0.5 V *vs.* Li$^+$/Li and the charge capacity has also increased to 720 mAhg^{-1} which in turn means the irreversible capacity loss has decreased to 23%.

In the third activation cycle, the voltage profile exhibits even more well-defined features, clearly showing a higher degree of utilization of the Li—Si electrochemical alloying process. During the CC part of the lithiation process, the obtained capacity now reaches $\sim$650 mAhg^{-1}. In the following CV step the magnitude of the current response is somewhat decreased as compared to the first two cycles, which is to be expected since a significant part of the Li—Si electrochemical alloying reaction has now taken place above the cut-off voltage of 2 mV *vs.* Li$^+$/Li. It is also worth noting that the fluctuations in the measured current are less pronounced, possibly indicating stabilization of the SEI layer. At the end of the third CV step at 2 mV *vs.* Li$^+$/Li the capacity reaches $\approx$1040 mAhg^{-1}. The subsequent delithiation process again yields a well-pronounced plateau in the voltage profile and it was possible to extract Li-ions corresponding to a capacity of $\approx$890 mAhg^{-1} thereby lowering the irreversible loss to 15%.

The final two activation cycles (cycles 4–5) are a continuation of the trend exhibited by the three previous cycles in the sense that the plateaus in the voltage profiles become more well-defined and most of the capacity become accessible during the CC steps in the procedure. The current responses in the CV steps show significantly decreased magnitudes and almost approach zero at a relatively quick rate, which means the silica electrode can be considered to have become more or less fully activated under these conditions. During the holding steps of the 4th and 5th cycle the currents do not display any significant fluctuations, but decay rather smoothly, which could be an indication that a stable SEI has been formed on the electrode surface.

To further highlight the fact that electrochemical reduction of silica into elemental silicon actually takes place, the differential capacity plots displayed in Fig. 4b provide support for this claim *via* the gradual appearance of distinct features corresponding to the well-known red-ox potentials associated with the step-wise electrochemical alloying between lithium and silicon, namely at $\approx$0.2 and $\approx$0.06 V during lithiation and at $\approx$0.3 and $\approx$0.5 V during delithiation [45]. The differential capacity plot also highlights more clearly the reduction peaks in the voltage range of 0.7–1 V during the first cycle, which correspond to electrolyte decomposition and concurrent formation of an SEI layer on the electrode surface.

Fig. 5 displays the capacities obtained during the activation procedure, split into the galvanostatic and potentiostatic contributions. A comparison is made between carbon-coated and uncoated silica. It is evident that the available capacity in the C-coated sample during the galvanostatic step increases and converges toward a higher value than the non-coated sample. During the potentiostatic steps, the lithiation capacity of the SiO$_2$/C sample decreases with each activation cycle,
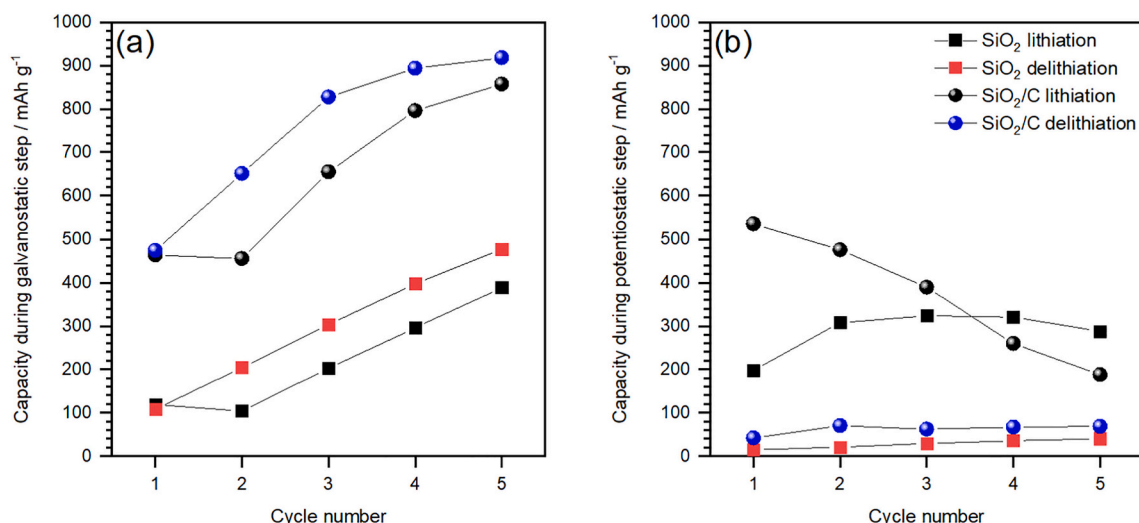
Fig. 5. Gravimetric capacities during the electrochemical activation procedure split into (a) charge passed during the galvanostatic steps, and (b) charge passed during the potentiostatic steps of the SiO_2 and SiO_2/C electrodes.

indicating that the carbon facilitates the activation procedure. The beneficial effect of a carbon coating will be further elaborated upon in Section 3.3.

3.4. Further half-cell characterization of electrochemically activated diatom-derived anodes and the effect of a C-coating

The electrochemical properties of pre-conditioned silica-based anodes, both non-coated and carbon coated frustules, are summarized in Fig. 6. The voltage profiles of the activation cycles are displayed side-by-side in Fig. 6a, b for a direct comparison. The most obvious difference between the non-coated and carbon coated frustules is that the latter delivers higher reversible capacities, and the activation appears to proceed quicker compared to its non-coated counterpart. The quasi-plateaus at <1 V vs. Li^+/Li that are associated with the electrochemical (de)alloying reaction between Li and Si also become significantly more pronounced. Moreover, a closer inspection of the voltage profiles reveals slightly more sloping curves in the C-coated samples. Insertion of Li-ions into amorphous carbon blacks or hard carbons occurs over a wide voltage range due to their porous and disordered structures. The reversible Li-storage capacities of carbon blacks using $LiPF_6$ in EC: DEC as electrolyte typically range between 100 and 275 $mAhg^{-1}$ [38,46]. Since the electrodes consist of only 10 wt-% carbon black, the capacity contribution from this additive is small. In the not C-coated electrodes, the effect of carbon black is therefore minimal in terms of its contribution and visible features in the voltage profiles, and the overall lack of conductive carbon ultimately results in relatively low Li-storage capacities. On the other hand, the effect of pyrolyzed carbon (15.4 wt-%) on the coated silica particles is visible under these experimental conditions, as evidenced by slightly more sloping voltage profiles in the 1–2 V range vs. Li^+/Li. Given the higher surface area of the SiO_2/C composite, the total capacity contribution of the pyrolyzed carbon may add up to 70–110 $mAhg^{-1}$ [38], which is measurable here. Although the signature is still dominated by the $Li_xSi \rightarrow Si + xLi^+ + xe^-$ electrochemical alloying reaction, it has been proposed that the electrochemical activity of $Li_2Si_2O_5$ also contributes here [31], albeit to a lesser extent, which would manifest itself as a somewhat smeared out voltage profile. Furthermore, such sloping voltage profiles observed here are also typically featured in SiO_x/C composites [28,47], thus providing more evidence for electrochemical reduction of the silica in the C-coated samples.

Rate capability tests on the pre-conditioned electrodes were also performed. Fig. 6c, d shows a comparison of the voltage profiles of

pristine frustules and C-coated frustules at various applied current densities. The tests were performed after both electrodes had underwent the previously described activation procedure. At first, the cells were cycled at a slow rate by applying currents of magnitude 50 mAg^{-1}. The current was then gradually increased in sequence after intervals of 10 cycles up to a value of 2000 mAg^{-1}. With each increment in applied current density, the accessible capacity is progressively lowered and the voltage polarization between the lithiation and delithiation processes increases as well. At the 10th cycle in each current density regime, the non-coated frustules have gravimetric delithiation capacities of 473, 469, 446, 371, 303 and 223 $mAhg^{-1}$ (at 50, 100, 200, 500, 1000 and 2000 mAg^{-1}), respectively. At the slowest cycling rate (i.e., 50 mAg^{-1}), the voltage hysteresis between the lithiation and delithation processes at ca. 50% SOC is $\approx$0.3 V. As the applied current density is increased to its highest (i.e., 2000 mAg^{-1}), the hysteresis increases accordingly to a value of $\approx$0.5 V. By comparison, the C-coated frustules exhibit higher overall Li-storage capacities for all current densities. Beginning with a slow cycling rate and gradually increasing the current density in the same manner as previously described, the obtained delithiation capacities are 792, 753, 697, 616, 545 and 451 $mAhg^{-1}$. The presence of a carbon coating is thus clearly beneficial both in terms of facilitating the activation of the material and its ability to deliver higher capacity at higher rates. However, the voltage hysteresis is barely affected by the application of a carbon coating, suggesting that the lithiation/delithiation of the bulk silica-based matrix is a limiting factor.

The evolution of the gravimetric (de)lithiation capacities of both non-coated and C-coated frustules as a function of cycle number are shown in Fig. 6e, f. Over the course of 100 cycles at a current density of 100 mAg^{-1}, it appears that the C-coated frustules exhibit a relatively stable cycling performance, as witnessed by only a slow and gradual loss in capacity. Here, it is relevant to make a comparison to pure Si electrodes, which have a tendency to fail rather quickly without specific engineering of particle size/morphology and the use of stabilizing or film-forming additives such as fluoroethylene carbonate (FEC) or vinylene carbonate (VC) when electrochemically cycled to a deeply lithiated state vs. Li^+/Li [48–50]. The failure-mode of Si electrodes is complex, but the large volume expansion (>300%) during uptake of Li-ions which lead to particle cracking along with excessive electrolyte decomposition and a loss of electronic contact within the composite electrode are all common explanations for such a behavior. This highlights one of the proposed advantages of conversion-based electrode materials, since some of the inactive reaction products are believed to be able to buffer some of the strain and stress associated with the significant
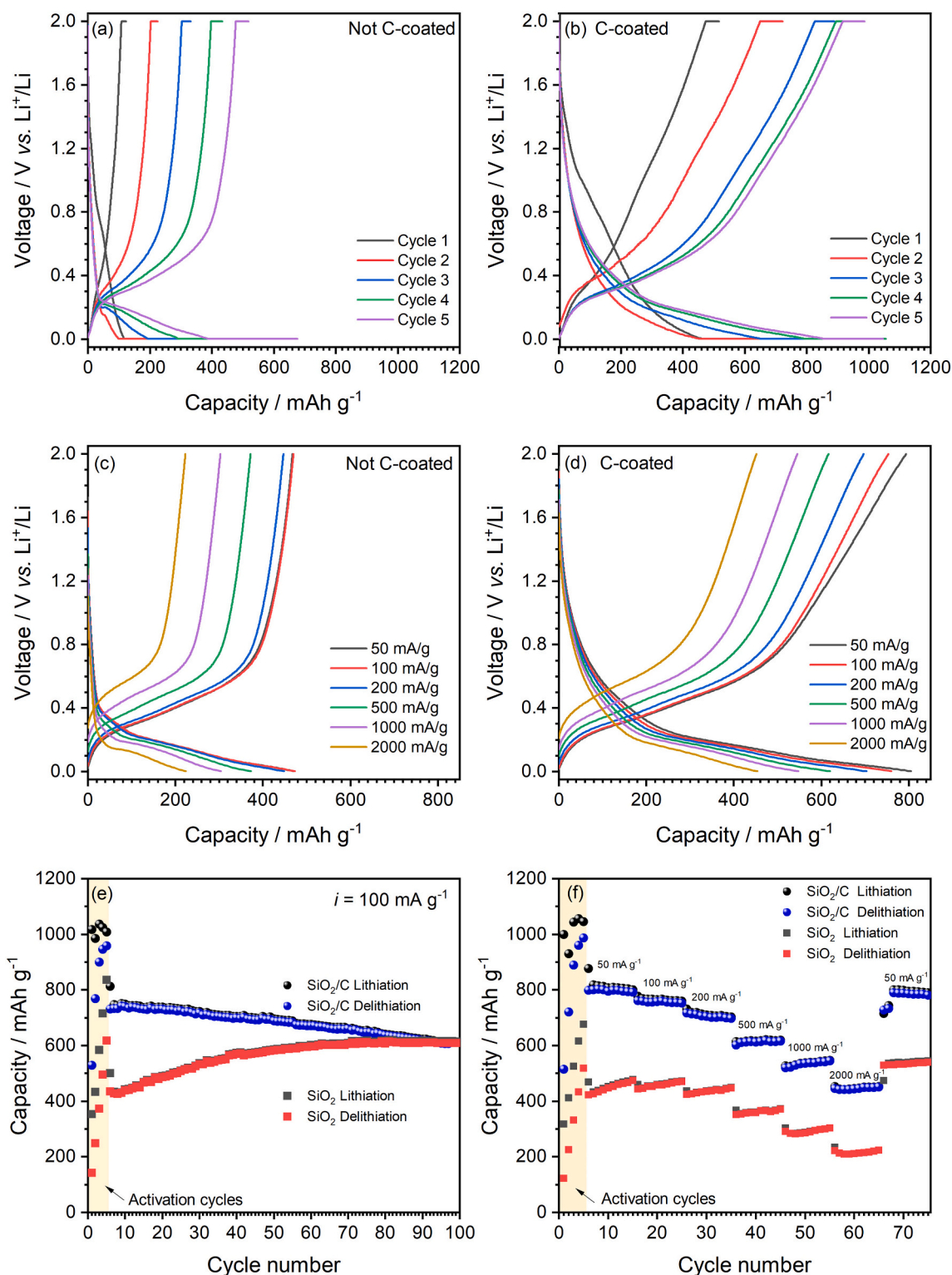
Fig. 6. Summary of the galvanostatic lithiation-delithiation cycles comparing crushed non-coated and carbon-coated frustules in half cells. (a) Voltage profiles of the first five activation cycles, which include potentiostatic holding steps, of non-coated frustules. (b) An analogous visualization of the voltage profiles of the activation cycles of carbon-coated frustules. (c) Voltage profiles of non-coated frustules at various current densities. (d) Voltage profiles of the C-coated frustules at various applied currents. (e) Evolution of gravimetric capacities as a function of cycle number at a current density of 100 mAg^{-1}. (f) Rate test comparison between non-coated and carbon coated frustules.

volume expansion-contraction upon repeated (de)lithiation cycles. A porous carbon-coating may also have a similarly protective effect by inhibiting HF-etching of the silica when LiPF$_6$ is used as electrolyte salt [51].

Initially the reversible capacity of the non-coated frustules is significantly lower than that of the carbon-coated ones ($\approx$430 *vs.* $\approx$810 mAhg^{-1}). However, the capacity increases incrementally with each electrochemical lithiation/delithiation cycle until it reaches $\approx$614

mAhg^{-1} at the completion of the test. This is attributed to an effect in which the electrochemically active surface area is gradually increased as the depth of lithiation steadily grows in each lithiation cycle. The reaction reduces more and more of the SiO$_2$ in each cycle forced by repeated (de)conversion thereby leading to an increased storage capacity of Li-ions [52–54].

3.5. Half-cell properties of SiO$_2$/C activated by internal short circuiting

The electrochemical properties of a SiO$_2$/C electrode that was activated by internal short circuiting *via* direct contact with a piece of metallic Li foil is displayed in Fig. 7a–c. Overall, the properties are similar to the electrochemically activated electrodes discussed in earlier sections - both in terms of its voltage profiles, gravimetric capacities and rate susceptibility. The re-assembled half cell had an OCV of ≈0.1 V *vs.* Li$^+$/Li. An attempt was made to lithiate the electrode further ("Cycle 0" in Fig. 7a), but no additional lithiation capacity could be obtained, which indicates that the reaction was already complete. The reader is referred to the supplementary information file for more comparisons between the activation procedures.

3.6. Implementation of a silica-based anode in a lithium ion battery

Since the electrochemical properties of the carbon-coated frustules were more favorable than those of the non-coated ones, the SiO$_2$/C composite anode was chosen for further study in a full cell configuration with NMC as a cathode material. Since the SiO$_2$/C electrode activated *via* internal short circuiting showed slightly lower capacities and would furthermore have to be delithiated prior to full cell assembly, an electrochemically activated electrode was instead chosen out of convenience. The electrochemical properties of the NMC cathode were investigated separately in a Li half-cell configuration in order to ensure a reliable performance in terms of cycling stability, representative voltage profiles, acceptable coulombic efficiencies and so on, see Fig. S5.

3.6.1. Full cell behavior

The assembled cell comprising a pre-conditioned (electrochemically activated), delithiated anode and a fully lithiated (*i.e.,* pristine) NMC cathode had an open-circuit voltage (OCV) of ≈1.3 V and the voltage profiles of the first five cycles of the NMC||SiO$_2$/C cell are displayed in Fig. 8a. During the first charge, the cell voltage increases rapidly and adopts a sloping appearance (average potential ≈3.6 V) which is maintained to the upper cut-off at 4.2 V. The initial charge capacity of ≈171 mAhg^{-1}, here referred to with respect to the mass of active NMC, is in line with findings from the previous half-cell study. Note also that the voltage profile of the first charge does not exhibit any distinct features (*i.e.,* kinks or quasi-plateaus) in the cell voltage range of 2.7–3.1 V since electrolyte decomposition and SEI formation on the anode surface

has already taken place during the pre-conditioning procedure. While the possibility of additional SEI formation on the anode cannot be ruled out, such effects are not directly measurable as visible features in the full-cell voltage profile post-activation. In the first discharge, the cell delivers a specific capacity of ≈147 mAhg^{-1} at an average discharge voltage of ≈3.06 V. This corresponds to an energy density of 387 mWhg^{-1} (here referred to the total mass of active materials in both electrodes) and to a first cycle coulombic efficiency of ≈86% as well as an energy efficiency of ≈73%. Upon continued cycling of the full cell, the discharge capacity stabilizes somewhat at around ≈147 mAhg^{-1} during the first 10 cycles. While an increase of the coulombic efficiency is initially observed as well, it remains fluctuating around 99%. This unavoidably leads to a slow and gradual decrease in the reversible capacity (Fig. 8b.) of the cell since a non-negligible amount of the Li-inventory is irreversibly consumed due to some parasitic side-reactions in every cycle. After 50 cycles the discharge capacity drops to 118 mAhg^{-1}, which in turn corresponds to an energy density of 297 mWhg^{-1}. The evolution of the energy density delivered by the cell as a function of cycle number is displayed in Fig. 8c. The energy efficiency initially rises to ≈83% in the first few cycles, but then gradually drops and stabilizes at ≈81% upon prolonged cycling. A further elaboration on the evolution of the gravimetric storage capacity and energy density is made by monitoring the change of the average charge and discharge potentials as well as the gap between them. Here, the calculated values based on experimentally obtained energy densities and coulometric capacities are displayed in Fig. 8d. It can be seen that the average charge potential stabilizes relatively quickly at ≈3.56 V while the average discharge potential, on the other hand, drops from ≈3.06 to ≈2.93 V during the first 20 cycles. The effect is further highlighted by the corresponding change in voltage hysteresis which gradually increases to ≈0.63 V, hence a lower energy efficiency (≈81%) is finally observed.

It was necessary to set the lower voltage cut-off to 1.3 V (*i.e.,* a voltage comparable to OCV just after cell assembly) in order to relithiate the cathode and delithiate the anode. This necessity likely arises mainly due to the delithiation properties of the anode rather than lithiation of the cathode counterpart. More specifically, it is attributed to the relatively large overpotential required to achieve delithiation of the anode which is completed at >1.5 V *vs.* Li$^+$/Li. This effect is further manifested in energy efficiencies of ≈81% upon further cycling. Upon closer inspection of the discharge voltage profile one can qualitatively divide it into two regions, one above >3 V and another below <3 V. There is a minor inflection at roughly ≈60% depth of discharge. This region of the discharge process corresponds more or less to the process in which the dominating delithiation reaction in the negative electrode gradually approaches its completion. Since N/P ≈ 1, it is possible to check the individual half-cell profiles in order to gain some insight into what is going on. The relithiation profile of NMC is comparatively flat at this SOD (Fig. S5a), while the profile of the silica-based anode adopts a more
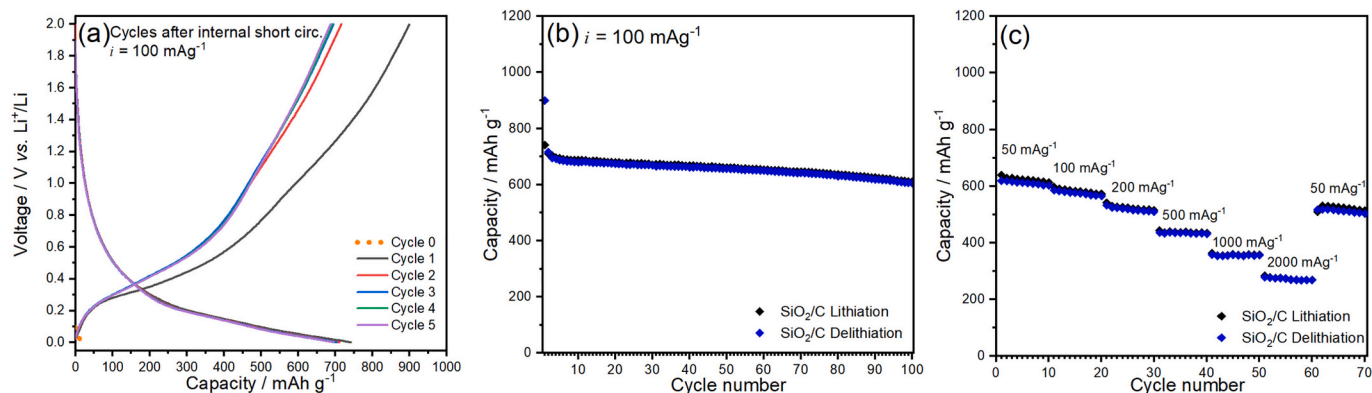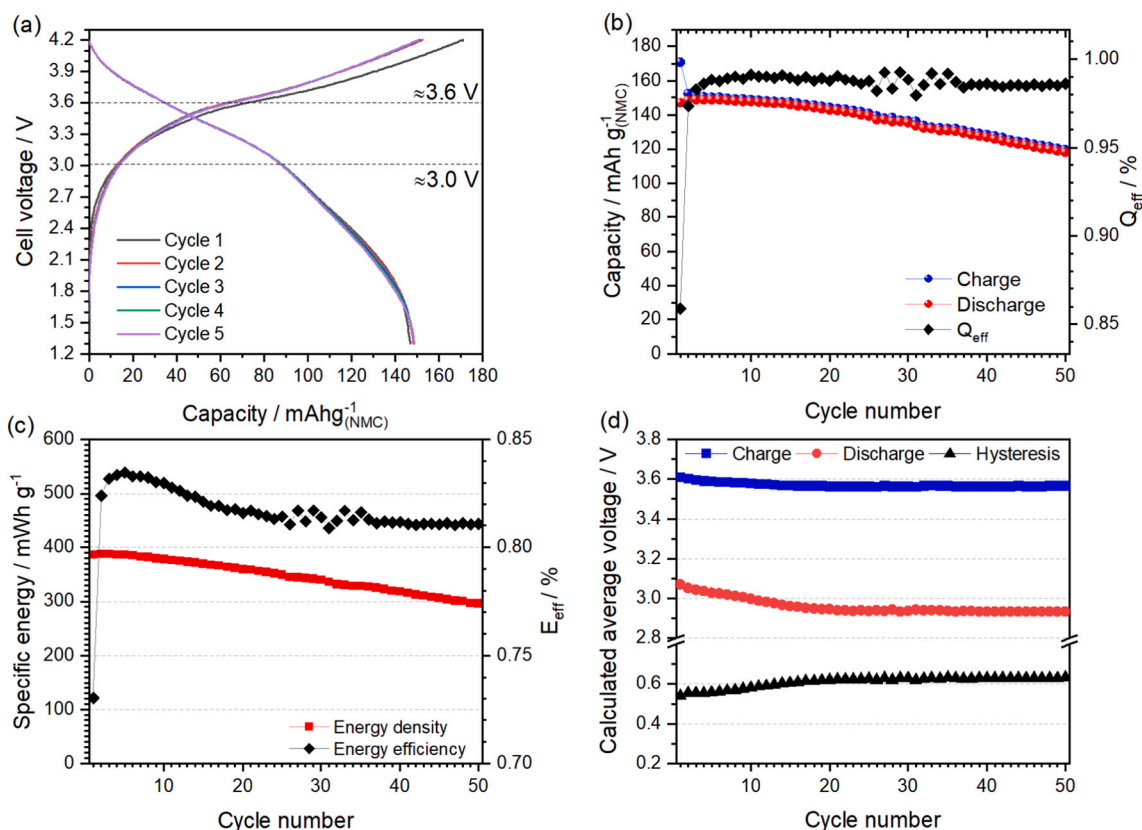

Fig. 7. Li half-cell performance of a SiO$_2$/C electrode activated by internal short circuiting *via* direct contact with Li metal. (a) Galvanostatic voltage profiles at 100 mAg^{-1}. (b) Gravimetric capacity evolution as a function of cycle number at 100 mAg^{-1}. (c) Rate capability test.

Fig. 8. Performance summary of the full cell containing and NMC cathode and a pre-conditioned SiO_2/C-based anode. (a) Voltage profiles during the first five charge-discharge cycles at C/10. Dashed lines indicate the average potentials of the charge and discharge processes. (b) Corresponding specific capacities and coulombic efficiencies of the full cell as a function of cycle number. (c) Energy density and energy efficiency plotted *versus* cycle number. (d) Evolution of the average charge and discharge voltages as well as the difference between them.

sloping profile with a slight increase in the rate of change of the voltage with respect to the amount of charges passed through the cell. There are several reasons for the sloping profile of the anode. Even if the conversion reactions ensure the formation of a composite where stable lithiaton and delithiation of Si is the main charge storage mechanism, the conductivity through the electrode is might still be insufficient. Furthermore, the delithiation of the carbon coating contributes to gives rise to such a behavior. It has also been proposed that the electrochemical activity of $Li_2Si_2O_5$ will contribute at higher anode potentials. Altogether, the presence of multiple electrochemically active species in the complex nanocomposite at the negative electrode ultimately has the effect of smearing out the voltage profile. Another way of putting it is that a range of active compounds (*i.e.*, Li_xSi, $Li_2Si_2O_5$, amorphous carbon *etc.*), perhaps also with a distribution in particle size, within the composite electrode that react simultaneously or in close sequence will give rise to a less well-defined cycling profile as the reactions take place over a wider voltage range, thereby requiring a rather low discharge cut-off voltage for the full cell.

For the sake of discussion, it should be noted that the first region (4.2–3 V) in the full cell voltage profile could in principle be extended by simply decreasing the N/P ratio (*i.e.*, utilizing a significantly oversized anode). However, this would come at the expense of effectively increasing the amount of dead weight within the anode composite electrode as well. While the energy efficiency could be improved in such an approach, the total energy density would be reduced when considering the electrodes masses as a whole, and is therefore less relevant for further studies, particularly since electrochemical activation is clearly a more limiting factor here. It is suggested that perhaps a more fruitful approach for SiO_2 and SiO_X-based anodes could be to investigate whether it is possible to more carefully control the electrode

composition *via* some clever pre-lithiation procedure or other pretreatment that maximizes the amount of active components (*e.g.*, Li_xSi) while simultaneously minimizes the amount of inactive components (*e.g.*, Li_2O, Li_4SiO_4).

4. Conclusions

Silica derived from a natural resource, namely algae, can be processed and used as an electrode material which reacts reversibly with Liions at low potentials *vs.* Li^+/Li. Electrodes with a high silica content (75 wt%) were subjected to a particular electrochemical activation procedure which ensures a high degree of conversion of the silica at a low potential *vs.* Li^+/Li. It is demonstrated that time spent at a low potential is a crucial factor in the activation of the material, and that a carbon-coating appears to significantly facilitate the process. It is further demonstrated that prelithiation by internal short circuiting in a cell with direct contact between the silica electrode and metallic lithium gives an almost identical degree of conversion. A full cell comprising an electrochemically precondintioned SiO_2/C-based anode and a NMC 442 cathode was assembled and tested. On the basis of the amount active materials only, such a full cell has an initial (discharge) energy density of 387 $mWhg^{-1}$ and an energy efficiency of $\approx$83% that both gradually drops with continued cycling. Despite exhibiting large gravimetric capacities (in relation to conventional graphite anodes), and the excellent cycling stability in half cell, these silica-based anodes have intrinsic shortcomings that is the energy penalty associated with its relatively high delithiation potential, as well as the coulombic efficiency.

Declaration of Competing Interest

There are no conflicts to declare.

Acknowledgements

Appendix A. Supplementary data

Supplementary data to this article can be found online at https://doi.org/10.1016/j.ssi.2021.115766.

References

[1] J.-M. Tarascon, M. Armand, Issues and challenges facing rechargeable lithium batteries, Nature 414 (2001) 359–367, https://doi.org/10.1038/35104644.

[2] M. Armand, J.-M. Tarascon, Building better batteries, Nature 451 (2008) 652–657, https://doi.org/10.1038/451652a.

[3] Y. Nishi, Lithium ion secondary batteries; past 10 years and the future, J. Power Sources 100 (2001) 101–106, https://doi.org/10.1016/S0378-7753(01)00887-4.

[4] R. Fong, U. von Sacken, J.R. Dahn, Studies of lithium intercalation into carbons using nonaqueous electrochemical cells, J. Electrochem. Soc. 137 (1990) 2009, https://doi.org/10.1149/1.2086855.

[5] J.R. Dahn, A.K. Sleigh, H. Shi, et al., Dependence of the electrochemical intercalation of lithium in carbons on the crystal structure of the carbon, Electrochim. Acta 38 (1993) 1179–1191, https://doi.org/10.1016/0013-4686(93)80048-5.

[6] R. Yazami, P. Touzain, A reversible graphite-lithium negative electrode for electrochemical generators, J. Power Sources 9 (1983) 365–371, https://doi.org/10.1016/0378-7753(83)87040-2.

[7] Commission Staff, Commission Staff Working Document - Report on Raw Materials for Battery Applications, 2018.

[8] European-Commisson, On the Review of the List of Critical Raw Materials for the EU and the Implementation of the Raw Materials Initiative, 2014 (COM (2014)).

[9] R. Moss, E. Tzimas, P. Willis, et al., Critical Metals in the Path towards the Decarbonisation of the EU Energy Sector, 2013.

[10] A.N. Dey, Electrochemical alloying of Lithium in organic electrolytes, J. Electrochem. Soc. 118 (1971) 1547, https://doi.org/10.1149/1.2407783.

[11] P. Poizot, S. Laruelle, S. Grugeon, et al., Nano-sized transition-metal oxides as negative-electrode materials for lithium-ion batteries, Nature 407 (2000) 496–499, https://doi.org/10.1038/35035045.

[12] H. Li, P. Balaya, J. Maier, Li-storage via heterogeneous reaction in selected binary metal fluorides and oxides, J. Electrochem. Soc. 151 (2004) A1878, https://doi.org/10.1149/1.1801451.

[13] Y.F. Zhukovskii, E.A. Kotomin, P. Balaya, J. Maier, Enhanced interfacial lithium storage in nanocomposites of transition metals with LiF and Li2O: comparison of DFT calculations and experimental studies, Solid State Sci. 10 (2008) 491–495, https://doi.org/10.1016/j.solidstatesciences.2007.12.030.

[14] H. Huang, E.M. Kelder, L. Chen, J. Schoonman, Electrochemical characteristics of Sn1-xSixO2 as anode for lithium-ion batteries, J. Power Sources 81–82 (1999) 362–367, https://doi.org/10.1016/S0378-7753(98)00219-5.

[15] F. Lepoivre, D. Larcher, J. Tarascon, Electrochemical activation of silica for enhanced performances of Si-based electrodes, J. Electrochem. Soc. 163 (2016) A2791–A2796, https://doi.org/10.1149/2.1221613jes.

[16] B. Gao, S. Sinha, L. Fleming, O. Zhou, Alloy formation in nanostructured silicon, Adv. Mater. 13 (2001) 816–819, https://doi.org/10.1002/1521-4095(200106)13:11<816::AID-ADMA816>3.0.CO;2-P.

[17] Z. Liu, Q. Yu, Y. Zhao, et al., Silicon oxides: a promising family of anode materials for lithium-ion batteries, Chem. Soc. Rev. 48 (2019) 285–309, https://doi.org/10.1039/c8cs00441b.

[18] C.-W. Wang, K.-W. Liu, W.-F. Chen, et al., Mesoporous SiO 2 /carbon hollow spheres applied towards a high rate-performance Li-battery anode, Inorg. Chem. Front. 3 (2016) 1398–1405, https://doi.org/10.1039/C6QI00125D.

[19] P. Lv, H. Zhao, J. Wang, et al., Facile preparation and electrochemical properties of amorphous SiO2/C composite as anode material for lithium ion batteries, J. Power Sources 237 (2013) 291–294, https://doi.org/10.1016/j.jpowsour.2013.03.054.

[20] H. Li, X. Wu, H. Sun, et al., Dual-porosity SiO 2 /C Nanocomposite with enhanced lithium storage performance, J. Phys. Chem. C 119 (2015) 3495–3501, https://doi.org/10.1021/jp511435w.

[21] X. Cao, X. Chuan, R.C. Massé, et al., A three layer design with mesoporous silica encapsulated by a carbon core and shell for high energy lithium ion battery anodes, J. Mater. Chem. A 3 (2015) 22739–22749, https://doi.org/10.1039/c5ta05879a.

[22] Z. Xiang, Y. Chen, J. Li, et al., Submicro-sized porous SiO2/C and SiO2/C/graphene spheres for lithium ion batteries, J. Solid State Electrochem. 21 (2017) 2425–2432, https://doi.org/10.1007/s10008-017-3566-7.

[23] Y. Yao, J. Zhang, L. Xue, et al., Carbon-coated SiO2nanoparticles as anode material for lithium ion batteries, J. Power Sources 196 (2011) 10240–10243, https://doi.org/10.1016/j.jpowsour.2011.08.009.

[24] J.Y. Kim, D.T. Nguyen, J.S. Kang, S.W. Song, Facile synthesis and stable cycling ability of hollow submicron silicon oxide-carbon composite anode material for Li-ion battery, J. Alloys Compd. 633 (2015) 92–96, https://doi.org/10.1016/j.jallcom.2015.01.309.

[25] X. Yang, H. Huang, Z. Li, et al., Preparation and lithium-storage performance of carbon/silica composite with a unique porous bicontinuous nanostructure, Carbon NY 77 (2014) 275–280, https://doi.org/10.1016/j.carbon.2014.05.030.

[26] Y. Liang, L. Cai, L. Chen, et al., Silica nanonetwork confined in nitrogen-doped ordered mesoporous carbon framework for high-performance lithium-ion battery anodes, Nanoscale 7 (2015) 3971–3975, https://doi.org/10.1039/c4nr06611a.

[27] S. Hao, Z. Wang, L. Chen, Amorphous SiO 2 in tunnel-structured mesoporous carbon and its anode performance in Li-ion batteries, Mater. Des. 111 (2016) 616–621, https://doi.org/10.1016/j.matdes.2016.09.020.

[28] C. Gao, H. Zhao, P. Lv, et al., Superior cycling performance of SiOx/C composite with arrayed mesoporous architecture as anode material for lithium-ion batteries, J. Electrochem. Soc. 161 (2015) A2216–A2221, https://doi.org/10.1149/2.0911414jes.

[29] H.H. Li, L.L. Zhang, C.Y. Fan, et al., A plum-pudding like mesoporous SiO2/flake graphite nanocomposite with superior rate performance for LIB anode materials, Phys. Chem. Chem. Phys. 17 (2015) 22893–22899, https://doi.org/10.1039/c5cp03505h.

[30] G. Lener, M. Otero, D.E. Barraco, E.P.M. Leiva, Energetics of silica lithiation and its applications to lithium ion batteries, Electrochim. Acta 259 (2018) 1053–1058, https://doi.org/10.1016/j.electacta.2017.10.126.

[31] W.-S. Chang, C.-M. Park, J.-H. Kim, et al., Quartz (SiO2): a new energy storage anode material for Li-ion batteries, Energy Environ. Sci. 5 (2012) 6895, https://doi.org/10.1039/c2ee00003b.

[32] Q. Sun, B. Zhang, Z.W. Fu, Lithium electrochemistry of SiO2 thin film electrode for lithium-ion batteries, Appl. Surf. Sci. 254 (2008) 3774–3779, https://doi.org/10.1016/j.apsusc.2007.11.058.

[33] B. Guo, J. Shu, Z. Wang, et al., Electrochemical reduction of nano-SiO2 in hard carbon as anode material for lithium ion batteries, Electrochem. Commun. 10 (2008) 1876–1878, https://doi.org/10.1016/j.elecom.2008.09.032.

[34] M.N. Obrovac, V.L. Chevrier, Alloy negative electrodes for Li-ion batteries, Chem. Rev. 114 (2014) 11444–11502.

[35] A. Lisowska-Oleksiak, A.P. Nowak, B. Wicikowska, Aquatic biomass containing porous silica as an anode for lithium ion batteries, RSC Adv. 4 (2014) 40439–40443, https://doi.org/10.1039/C4RA06420H.

[36] A.P. Nowak, A. Lisowska-Oleksiak, B. Wicikowska, M. Gazda, Biosilica from sea water diatoms algae—electrochemical impedance spectroscopy study, J. Solid State Electrochem. 21 (2017) 2251–2258, https://doi.org/10.1007/s10008-017-3561-z.

[37] A.P. Nowak, M. Sprynskyy, W. Brzozowska, A. Lisowska-Oleksiak, Electrochemical behavior of a composite material containing 3D-structured diatom biosilica, Algal Res. 41 (2019) 101538, https://doi.org/10.1016/j.algal.2019.101538.

[38] A.N. Norberg, N.P. Wagner, H. Kaland, et al., Silica from diatom frustules as anode material for Li-ion batteries, RSC Adv. 9 (2019) 41228–41239, https://doi.org/10.1039/C9RA07271C.

[39] Z.H. Aitken, S. Luo, S.N. Reynolds, et al., Microstructure provides insights into evolutionary design and resilience of *Coscinodiscus* sp. frustule, Proc. Natl. Acad. Sci. 113 (2016) 2017–2022, https://doi.org/10.1073/pnas.1519790113.

[40] Y. Xing, L. Yu, X. Wang, et al., Characterization and analysis of Coscinodiscus genus frustule based on FIB-SEM, Prog. Nat. Sci. Mater. Int. 27 (2017) 391–395, https://doi.org/10.1016/j.pnsc.2017.04.019.

[41] S. Cicco, D. Vona, R. Gristina, et al., Biosilica from living diatoms: investigations on biocompatibility of bare and chemically modified *Thalassiosira weissflogii* silica shells, Bioengineering 3 (2016) 35, https://doi.org/10.3390/bioengineering3040035.

[42] K. Umemura, Y. Noguchi, T. Ichinose, et al., Morphology and physical-chemical properties of baked nanoporous frustules, J. Nanosci. Nanotechnol. 10 (2010) 5220–5224, https://doi.org/10.1166/jnn.2010.2400.

[43] L. Cao, J. Huang, Z. Lin, et al., Amorphous SiO2/C composite as anode material for lithium-ion batteries, J. Mater. Res. 33 (2018) 1219–1225, https://doi.org/10.1557/jmr.2017.298.

[44] M.V. Blanco, V. Renman, J. Zhu, et al., Optimizing carbon coating parameters for obtaining SiO2/C anodes with improved electrochemical performance, J. Solid State Electrochem. 25 (2021) 1339–1351, https://doi.org/10.1007/s10008-021-04912-2.

[45] M.J. Loveridge, M.J. Lain, I.D. Johnson, et al., Towards high capacity Li-ion batteries based on silicon-graphene composite anodes and sub-micron V-doped LiFePO 4 cathodes, Sci. Rep. 6 (2016) 1–11, https://doi.org/10.1038/srep37787.

[46] K.A. See, M.A. Lumley, G.D. Stucky, et al., Reversible capacity of conductive carbon additives at low potentials: caveats for testing alternative anode materials for Li-ion batteries, J. Electrochem. Soc. 164 (2017) A327–A333, https://doi.org/10.1149/2.0971702jes.

[47] G.A. Elia, J. Hassoun, A SiOx-based anode in a high-voltage lithium-ion battery, ChemElectroChem 4 (2017) 2164–2168, https://doi.org/10.1002/celc.201700316.

[48] N.S. Choi, K.H. Yew, K.Y. Lee, et al., Effect of fluoroethylene carbonate additive on interfacial properties of silicon thin-film electrode, J. Power Sources 161 (2006) 1254–1259, https://doi.org/10.1016/j.jpowsour.2006.05.049.

[49] T. Jaumann, J. Balach, M. Klose, et al., SEI-component formation on sub 5 nm sized silicon nanoparticles in Li-ion batteries: the role of electrode preparation, FEC

addition and binders, Phys. Chem. Chem. Phys. 17 (2015) 24956–24967, https://doi.org/10.1039/c5cp03672k.

[50] T. Jaumann, J. Balach, U. Langklotz, et al., Lifetime vs. rate capability: understanding the role of FEC and VC in high-energy Li-ion batteries with nano-silicon anodes, Energy Storage Mater. 6 (2017) 26–35, https://doi.org/10.1016/j.ensm.2016.08.002.

[51] B. Philippe, R. Dedryvère, M. Gorgoi, et al., Improved performances of nanosilicon electrodes using the salt LiFSI: a photoelectron spectroscopy study, J. Am. Chem. Soc. 135 (2013) 9829–9842, https://doi.org/10.1021/ja403082s.

[52] P. Poizot, S. Laruelle, S. Grugeon, et al., Searching for new anode materials for the Li-ion technology: time to deviate from the usual path, J. Power Sources 97–98 (2001) 235–239, https://doi.org/10.1016/S0378-7753(01)00508-0.

[53] S. Grugeon, S. Laruelle, R. Herrera-Urbina, et al., Particle size effects on the electrochemical performance of copper oxides toward lithium, J. Electrochem. Soc. 148 (2001) 285–292, https://doi.org/10.1149/1.1353566.

[54] Y. Yu, Y. Shi, C.H. Chen, Nanoporous cuprous oxide/lithia composite anode with capacity increasing characteristic and high rate capability, Nanotechnology 18 (2007), https://doi.org/10.1088/0957-4484/18/5/055706.